9

High Resolution Magnetic Imaging by Local Tunneling Magnetoresistance

W. Wulfhekel

An introduction to spin-polarized scanning tunneling microscopy with a soft magnetic tip is given. After illustrating the fundamental physical effect of tunneling magnetoresistance and giving a short historical background, it is shown how magnetic and topographic information can be separated using a modulation technique of the tip magnetization. Important for the functionality of the method is to avoid magnetostriction in the tip during reversal of its magnetization. It is shown that this is theoretically and experimentally possible with an appropriate tip material of very low magnetostriction. The closure domain structure of Co(0001) is studied and ultrasharp 20° domain walls of only 1.1 nm width are found. This narrow width is explained on the basis of a micromagnetic model, and a lateral resolution of the technique better than 1 nm is shown. The limits of the technique due to the stray field of the magnetic tip are illustrated. In the case that the stray field of the tip influences the sample under investigation, the local magnetic susceptibility can be measured. Furthermore, we focus on the contrast mechanism and give evidence that the tunneling magnetoresistance depends on the barrier height in agreement with Slonczewski's model. Finally, the possibility of magnetic imaging through a non-magnetic overlayer is discussed.

9.1 Introduction

Since the invention of scanning tunneling microscopy (STM) in 1981 by Binning and Rohrer [1], the technique has developed into an invaluably powerful surface analysis tool due to its real space imaging capabilities with atomic resolution [2]. Working in the field of magnetic imaging, one may ask the simple question: Is it possible to develop a technique similar to STM to image magnetic domains with high resolution? The invention of spin-polarized scanning tunneling microscopy (SP-STM) is the direct answer to this question. In an SP-STM not only is the electron charge used to map the surface topography, but also the electron spin is utilized to image the spin structure of the sample, which is directly related to the sample magnetization. The principle of operation of an SP-STM is based on a fundamental property of ferromagnets. Due to the spin-sensitive exchange interaction between localized electrons

(Heisenberg model) or electrons in a delocalized electron gas (Stoner model), the electronic density of states splits up into different minority and majority densities (Fig. 9.1a). This is in contrast to paramagnetic substances, where the distributions of spin-up and spin-down electrons are identical. It was Jullière [3] who discovered in 1975 the consequences of this imbalance of majority and minority electrons, i.e., the spin polarization, on tunneling between two ferromagnets. In his fundamental experiment, two magnetic films, Fe and Co, were isolated by a thin Ge film to form a tunnel junction. The two magnetic films had the same easy axis of magnetization but different coercive fields. This permitted the alignment of their magnetization parallel or antiparallel as a function of an applied magnetic field. Jullière found that the tunneling conductance G depends on the relative orientation of the magnetization of the two layers. For parallel orientation, the conductance G was 14% higher than for antiparallel orientation. He explained his finding with the spin polarization of the tunneling electrons. Under the assumption of a small bias voltage across the junction and in the absence of spin-flip scattering during the tunneling process, the electrons in the ferromagnets near the Fermi energy determine the tunneling conductance of the junction. For a parallel orientation, the majority/minority electrons of the first electrode tunnel into the majority/minority states in the second electrode, respectively, as depicted in Fig. 9.1a. In the simple case that the transmission through the barrier material itself shows no spin dependence, the conductance $G_{\uparrow\uparrow}$ is proportional to the density N of initial and final states and hence is proportional to the product of the initial and final majority and minority densities:

$$G_{\uparrow\uparrow} \propto N_{\uparrow}(1)N_{\uparrow}(2) + N_{\downarrow}(1)N_{\downarrow}(2) \tag{9.1}$$

For antiparallel orientation of the magnetization (see Fig. 9.1b), majority/minority electrons tunnel into minority/majority states and the conductance $G_{\uparrow\downarrow}$ is proportional to:

$$G_{\uparrow\downarrow} \propto N_{\uparrow}(1)N_{\downarrow}(2) + N_{\downarrow}(1)N_{\uparrow}(2)\ . \tag{9.2}$$

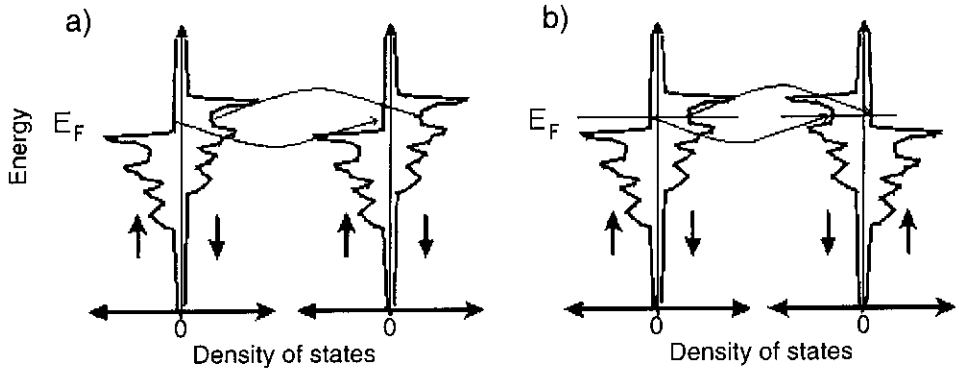

Fig. 9.1. Schematic drawing of spin-conserved tunneling between two ferromagnetic materials represented by their density of states. In (**a**) the two ferromagnets are magnetized parallel such that majority electrons from one electrode tunnel into minority states of the other electrode, while in (**b**) the ferromagnets are magnetized antiparallel such that majority electrons from one electrode tunnel into minority states of the other

With the spin polarization $P_i = (N_\uparrow(i) - N_\downarrow(i))/(N_\uparrow(i) + N_\downarrow(i))$ of the electrons of electrode i, the relative variation of the conductance is given by:

$$\Delta G/G_{\uparrow\uparrow} = 2P_1P_2/(1 + P_1P_2) \; . \tag{9.3}$$

This variation of the conductance and consequently of the resistance is called the tunneling magnetoresistance (TMR). More than a decade later, Slonczewski treated the problem of spin-polarized tunneling rigorously in the free electron model [4]. Neglecting higher order spin effects like spin accumulation, he calculated the dependence of the conductance on the angle θ between the magnetization of the two layers:

$$G = G_0(1 + P_1'P_2'\cos\theta) \; . \tag{9.4}$$

Where P_i' is the effective spin-polarization of the combination of ferromagnet i and the barrier, while G_0 is the mean conductance containing no parameters of the magnetization direction of the layers. The $\cos\theta$ dependence is strict, since it originates from the quantum mechanical rotation behavior of the spin $1/2$ tunneling electrons, i.e., it reflects the electron spin. Later, Slonczewski's prediction for the angular dependence of the TMR effect was also experimentally confirmed [5].

During the last decade, many attempts have been made to use the TMR effect in an STM to obtain spin sensitivity. Two different approaches have been of major importance: First, the use of ferromagnetic tips that lead to a spin-polarized tunneling according to Jullière's model discussed above, and, secondly, the use of GaAs tips with spin-polarized carriers that are created by optical pumping with circularly polarized light [6]. Early attempts in the beginning of the 1990s to use ferromagnetic tips and utilize the TMR effect were of limited success. The experiments by Johnson and Clarke [7], who used bulk Ni tips to image the magnetic structure of surfaces in air, were dominated by spurious effects like magnetostriction and mechanical vibrations of the tip or sample. Almost at the same time, Wiesendanger et al. [8] reported spin-polarized vacuum tunneling at room temperature between a ferromagnetic CrO_2 tip and the topological antiferromagnetic Cr(001) surface [9]. Using a tungsten tip, topographic constant current line scans revealed atomic steps on Cr(001) of the expected step height of 0.14 nm, while using a ferromagnetic CrO_2 tip, alternating step heights of 0.16 and 0.12 nm were observed. This was attributed to the TMR effect between the ferromagnetic tip and the ferromagnetically ordered Cr atoms on the terraces. When the spin polarization of the tip and the Cr terrace atoms are parallel, the tunneling current is enhanced due to the TMR effect (see Eq. 9.4) and in the constant current mode of the STM, the tip is retracted by a small amount (0.02 nm). On the adjacent atomic terrace on Cr, the spin polarization of the terrace atoms is opposite due to the topological antiferromagnetic order of Cr(001) [9]. Therefore, on this terrace, the TMR effect leads to a reduction of the current and the STM tip approaches. This mechanism results in alternating step heights seen with a spin polarized tip. However, no separation of topography and spin information could be obtained in this approach, and reference measurements had to be acquired with nonmagnetic tips.

In the mid-1990s, a more promising approach for magnetic imaging using optically pumped GaAs tips in combination with a lock-in technique to separate topographic and magnetic information was established [10–12]. By using circularly polarized light, spin polarized carriers are excited into the conduction band of the tip and then tunnel into the sample. The spin polarization of the electrons can be selected by the helicity of the light [6]. This is the key to separating spin information from topographic information. By modulating the helicity of the light, and by this the spin polarization of the carriers, modulations in the tunneling current are induced due to spin-dependent tunneling. The modulations were detected with a lock-in amplifier. The signal is used to construct magnetic images, as shown in Fig. 9.2. Hence, the modulation of spin polarization enables one to separate spin information (Fig. 9.2a) from topographic information (Fig. 9.2b), although only one physical parameter, i.e., the tunneling current, is measured. The spin information is contained in the AC part of the tunneling current at the frequency of the optical modulation, while the topographic information is contained in the DC component. This optical modulation technique, however, suffers from a rather low contrast. Further, an unintended additional magneto-optical contrast of limited lateral resolution is present due to the interaction of the light and the sample [13]. Only a few studies on domain patterns have been published using this technique, and no experiments have been presented

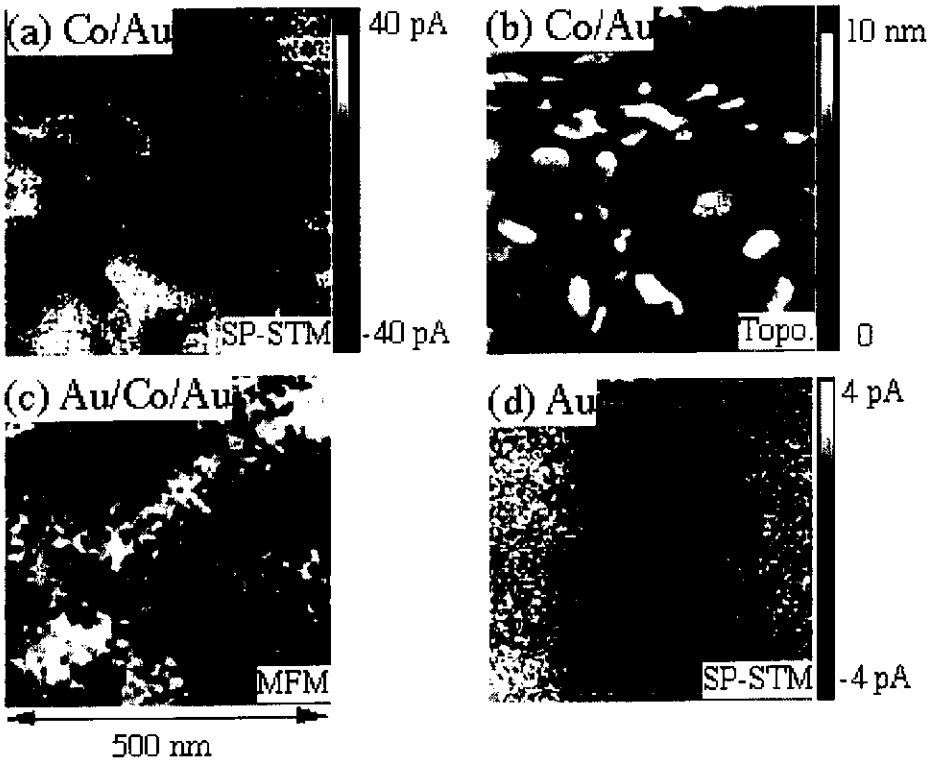

Fig. 9.2. (**a**) Magnetic SP-STM image and (**b**) topographic image of the same location of a Co film on Au. The polarization image shows magnetic domains that are similar to those obtained by MFM on a Au-covered sample depicted in (**c**). Magnetic SP-STM image of an Au film showing a non-vanishing contrast. All images are 0.5 × 0.5 μm. Figure taken from [14]

that rigorously prove the magnetic origin of the observed domains. Moreover, non-magnetic films are reported to show in some cases a considerable signal (see Fig. 9.2c) similar to the domains in magnetic films [14], raising questions about the reliability of this method.

Recently, different groups revived the first approach, the use of ferromagnetic tips. In these new approaches, spin and topographic information could be separated by two methods [15, 16]. Bode et al. used spin-polarized scanning tunneling spectroscopy to obtain spin information. This approach is described in detail in Chap. 10. The second method is addressed in the following section.

9.2 Experimental Setup

In this section, we focus on the use of ferromagnetic tips in combination with a modulation technique of the spin polarization. Analogous to the concept of optically pumped GaAs tips, a modulation of the spin polarization is used to separate spin information from topographic information in the tunneling current. In this approach to SP-STM, a soft magnetic tip is chosen as the STM tip. The longitudinal magnetization of the tip is switched periodically with the frequency f by the magnetic field induced by a small coil wound around the tip, as depicted in Fig. 9.3. The whole volume of the tip is ferromagnetic such that the reversal of the whole tip is driven by the field of the coil at the backside of the tip, and the apex is switched between the two energetically favored longitudinal magnetized states, as will be discussed in detail below. In this way, the spin polarization of the electrons at the tip apex is periodically reversed. Magnetic contrast is separated from the topographic information by phase-sensitive detection of the Fourier component of frequency f via a lock-in amplifier. Due to the local tunneling magnetoresistance effect between the magnetic tip and the surface of the specimen, the tunneling current shows an AC component related to the spin polarization of the sample. If the switching frequency f of the tip is chosen well above the cut-off frequency of the feedback loop of the STM, the variations in the tunneling current are not compensated by the current feedback loop and may be detected in the tunneling current with the lock-in amplifier. The DC component in the tunneling current is used to map the topography simultaneously with the spin structure. Important for the functionality of the method is that mechanical vibrations are avoided during the switching process of the tip and that the tip–sample distance is kept constant. Primarily, this is necessary to prevent the tip from crashing into the sample surface, since it is positioned only a few Å in front of the sample during STM operation. Secondly, one has to avoid changes in the tunneling current due to distance changes in order not to cover the small modulations of the tunneling current caused by the tunneling magnetoresistance. Due to the exponential dependence of the tunneling current on the gap width, the tolerable changes of the distance are only on the order of 0.05 Å. For larger mechanical vibrations, the variations in the tunneling current are larger than those caused by the TMR effect, which under favorable conditions is in the range of several 10% [17]. To achieve this low level of mechanical vibrations during the switching of the tip magnetization,

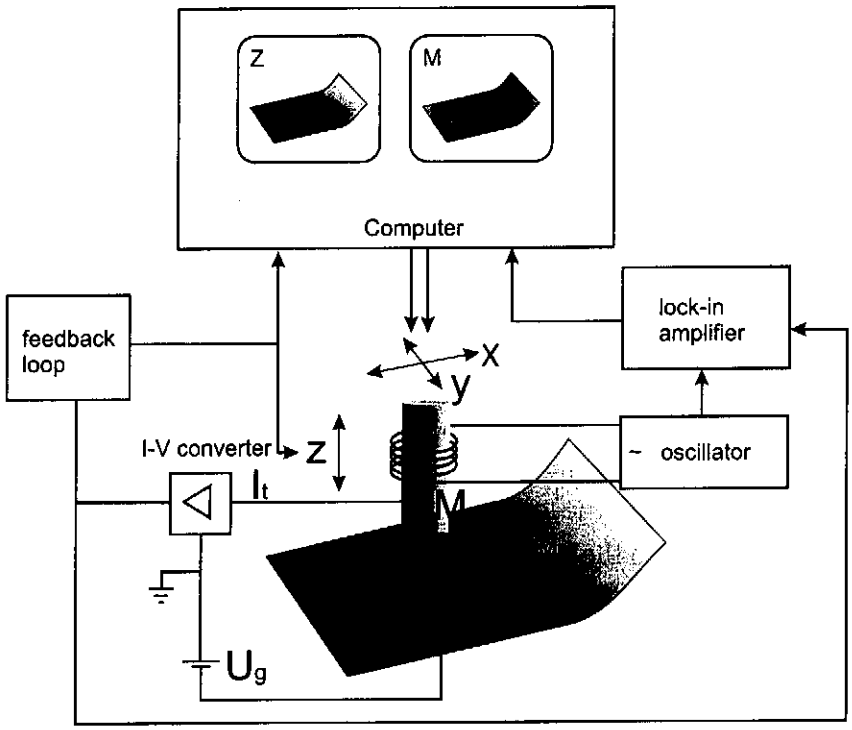

Fig. 9.3. Schematic drawing of the experimental setup. The magnetic tip of the STM can be scanned in x and y directions over the surface, while the z component is regulated with a constant current feedback loop such that the tip follows the topography of the sample. During scanning, the tip is periodically switched by the magnetic field of a coil wound around the tip. The resulting variations of the tunneling current are detected after preamplification with a lock-in amplifier to construct the magnetic image of the surface

special care has to be taken in the choice of the tip material. For optimal performance, one needs low coercive fields of the material to minimize magnetic dipolar forces between the tip and the exciting coil. Furthermore, a vanishing magnetostriction of the tip material prevents changes in the tip length during switching. Magnetization losses should be low to avoid energy dissipation and thus periodic heating and thermal expansion of the tip. Best results were obtained with an amorphous metallic glass of the CoFeSiB family with high Co concentration [18]. The material offers extremely low coercivities in the range of 50 μT with very high initial magnetic susceptibility, negligible magnetostriction ($< 4 \times 10^{-8}$) [19] and a low saturation magnetization of 0.5 T combined with low magnetization losses at frequencies up to 100 kHz.

The magnetic tips were electrochemically etched from specially designed thin CoFeSiB wires of 130 μm diameter. As etching agent, a dilute mixture of HCl and HF was used that was suspended by surface tension as a thin liquid membrane in a Pt ring during etching. The pH value was tuned such that the formation of silica from the Si in the amorphous wire was prevented. Using low etching currents on the order of 250 μA, sharp and pointed tips were created, as can be seen in Fig. 9.4a. The cone angle of the tip is typically between 8 and 15°, and the radius of curvature can be as low as 20 nm. These tips were then fixed with conducting glue to a nonmagnetic tip

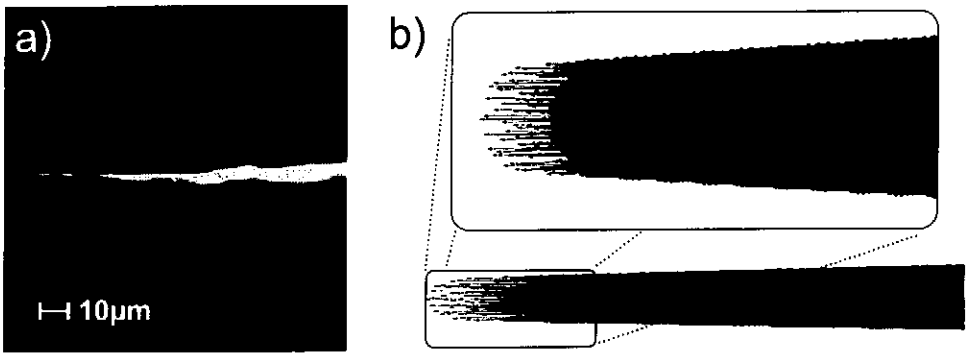

Fig. 9.4. (**a**) Scanning electron microscopy image of an etched CoFeSiB tip, (**b**) micromagnetic simulation of the tip magnetization. The inset shows the apex of the tip in higher magnification. The total length of the tip is 500 nm

shaft, around which the magnetic coil was wound. The coil was mechanically fixed to the shaft by insulating glue to avoid vibrations. The coil, which is used to switch the longitudinal magnetization of the tip, is sufficiently light, such that it can be scanned together with the tip during imaging of the surfaces.

9.3 Magnetic Switching and Magnetostriction of the Tip

To understand which magnetic information can be obtained with the soft magnetic tips, the magnetic configuration of the tip and its switching behavior were investigated. Micromagnetic calculations of the end of the tip were carried out to find the stable domain configuration. The simulations have been performed with a micro magnetic finite element algorithm based on direct energy minimization. The shape of the tip is approximated by a cone of an aperture angle of 12°, capped at its end with a hemisphere of 30 nm diameter. Since the whole magnetic tip is too large to be modeled in the framework of numerical micromagnetism, we analyzed only the last 500 nm of the end of the tip. This length, however, is well above the single domain particle diameter such that the end of the tip is free to form domains in the volume that is included in the simulations. As the stable configuration, we found the single domain state with a homogeneous magnetization pointing along the axis of the tip (see Fig. 9.4b) in agreement with what one would expect for an elongated object. The apex of the tip is free from vortices. On the outer surface of the cone-shaped tip, the magnetization points along the axis of the tip and hence does not lie in the surface of the tip. This can be explained by the limited saturation magnetization of the tip material. If the magnetization of the tip followed the contours of the cone, all the flux of the tip would be concentrated at the tip apex, where the flux would exceed the saturation of the material. However, the magnetization of the material is limited by the saturation magnetization, and the flux leaks out of the tip. This leaking keeps the magnetization exactly along the tip axis on the outer surface of the cone-shaped tip. Due to symmetry, the configuration of magnetization opposite than that depicted in Fig. 9.4b has the same energy. There are two stable configurations, and, therefore,

the end of the tip shows a bistable behavior. The switching of the magnetization of the tip is a more complex process. As has been shown using Kerr microscopy, the wires show a multidomain structure on the millimeter scale and lack a single, large Barckhausen jump [20]. Nevertheless, due to their extreme magnetic softness, they exhibit a high magnetic susceptibility. As a consequence, when a magnetic field is applied with the small coil at the backside of the tip, the flux created is dragged into the needle-shaped tip. Applying a field below saturation results in a movement of the internal 180° domain walls such that the flux induced by the coil at the backside is fully kept inside the tip. Magnetostatically, it is unfavorable for the flux to leak out at the side of the tip and instead it is guided to the apex. It is then only the direction of the flux that determines which of the two single domain configurations of the end of the tip is the more stable one. If pinning of domain walls does not hinder switching of the end of the tip, it is efficiently switched between the two states just by the collected flux from the backside of the tip. We confirmed this switching behavior of the tip by micromagnetic simulations that revealed no energetic barrier for domain wall motion in the vicinity of the tip apex and showed complete switching between two states of opposite longitudinal magnetization. In this way, sensitivity for the perpendicular component of the sample magnetization is achieved with our SP-STM. The simulations of the switching process also give an estimate of the expected magnetostriction of the tip during the process of switching. As switching of the tip proceeds by domain wall formation and movement and not by coherent rotation of the entire magnetization of the tip, magnetostriction is active in the magnetic domain walls only. Thereby, the length of the tip is changed by the magnetostriction in the wall, when it exits (or enters) the apex of the tip. The width of an 180° domain wall at the end of the tip is around 20 nm, as the micromagnetic calculations show. Together with the low magnetostriction constant of the material of $< 4 \times 10^{-8}$ this results in an undetectable distance change on the order of 10^{-5} Å. Theoretically, vibration due to magnetostriction can safely be neglected.

We checked experimentally for magnetostriction and other mechanical vibrations of the tip by performing test measurements of the SP-STM setup on a nonmagnetic Cu(001) sample. Figure 9.5a displays the topography of a Cu(001) crystal as obtained with a CoFeSiB tip while applying an alternating field of about 1 mT at 20 kHz. Terraces separated by atomic steps are clearly visible. Obviously, vibrations due to magnetostriction or other effects are small enough to get stable STM images. Note that the weak vibrations visible as ripples in the topography are not related to the switching of the tip, but are due to insufficient damping of vibrations of the building. In the signal obtained from the lock-in amplifier, however, one observes a weak contrast at the step edges (see Fig. 9.5b). This cross talk from the topography is on the order of 0.3% of the tunneling current and is due to small mechanical vibrations of the tip caused, e.g., by eddy currents acting on the tip in the alternating field of the coil. These vibrations can be avoided when the exciting field is reduced by one order of magnitude (see Fig. 9.5c and d). The lock-in signal using an exciting field of 100 μT is zero and does not show any crosstalk from the topography while the magnetization of the end of the tip is still switched, as will be discussed below. Hence, vibrations due to magnetostriction can be excluded down to the sensitivity

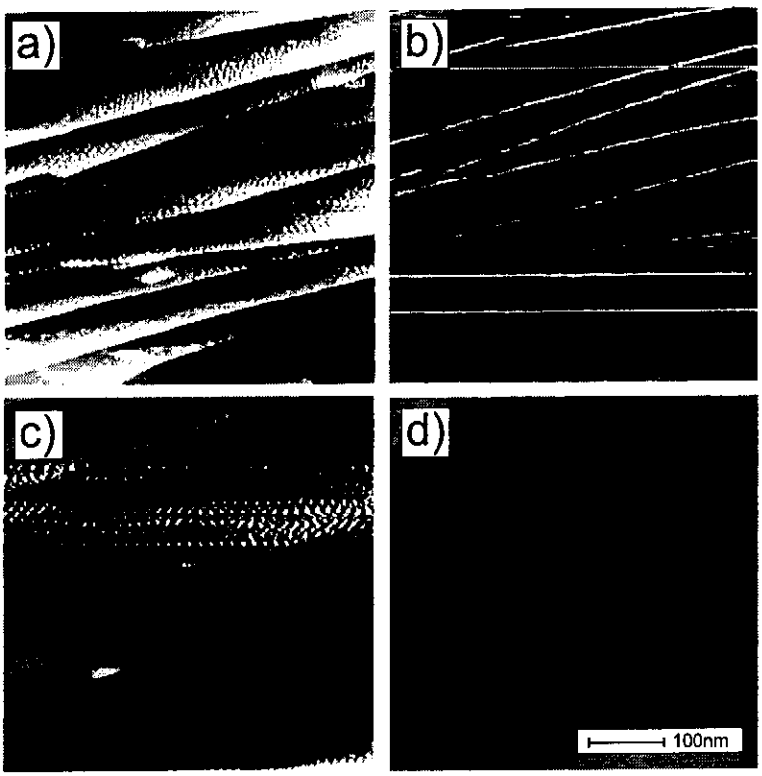

Fig. 9.5. (**a**), (**c**) STM scans of the topography and (**b**), (**d**) the spin signal of the same areas of Cu(001). During scanning an alternating magnetic field of 20 kHz was created by the coil around the tip. (**a**), (**b**) The field was set at 1.1 mT and (**c**), (**d**) 100 μT. For the higher field, mechanical vibrations of the tip are observed causing a cross-talk from the topography into the spin signal. (**b**), (**d**) Both spin images are normalized to a black and white contrast corresponding to 0.3% of the tunneling current

of the lock-in detection of $< 0.1\%$ of the tunneling current. Taking the well-known exponential dependence of the tunneling current on distance [21], one can estimate the vibrations in the narrow frequency bands around the modulation frequency f and its second harmonic. The lock-in signals correspond to distance changes between tip and sample of less than 5×10^{-4} Å, i.e., mechanical vibrations of the tip due to magnetostriction or other forces can experimentally be neglected. Using CoFeSiB, it is feasible to measure the tunneling magnetoresistance locally between the tip and the sample without unwanted mechanical vibrations.

9.4 Magnetic Imaging of Ferromagnets

Since the magnetic contrast of the SP-STM is based on the tunneling magnetoresistance effect, i.e., an interface effect, the instrument is mostly sensitive to the topmost atomic layer of the sample. As a consequence, atomically clean sample surfaces are required. The same holds for the apex of the tip. Therefore, the SP-STM experiments have to be performed in ultrahigh vacuum. After transferring new tips to the STM, the magnetic tips have to be cleaned in-situ by sputtering with 1 keV

Ar^+ ions to remove the native oxide at the apex. Samples were cleaned by cycles of argon sputtering (1 keV) and annealing until no traces of contamination could be found in Auger electron spectra. After sample and tip preparation, tunneling images of the topography, as well as the magnetization were recorded simultaneously at room temperature. After the initial tests for vibrations on a nonmagnetic substrate, we focused on imaging ferromagnetic surfaces. As a first example, a polished but polycrystalline Ni disk is imaged. On large scans (several μm^2) of the Ni surface, strong magnetic contrasts can be found in the spin signal, as displayed in Fig. 9.6a. The image of the spin signal shows two regions, i.e., domains with different intensities, separated by a fine, bright line, i.e., a domain wall. The observed domains in the spin signal are not related to the topography, as can be seen by comparing the topography of Fig. 9.6b with the spin signal of the very same area (white box in Fig. 9.6a). This excludes the possibility that the observed domains are caused by a crosstalk from the topography. In agreement with the theoretically predicted bistable behavior of the tip, the domains in the spin signal disappear abruptly when the size of the exciting field is lowered below 40 μT and reappear for fields above 50 μT. Upon further increase of the field, the contrast in the domain images does not rise further. The width of the domain walls observed on the polycrystalline Ni disk is between 100 and 150 nm and hence in qualitative agreement with calculated wall widths of 85–200 nm, depending on the wall type and the crystal orientation of Ni [22]. This gives a first hint of the good lateral magnetic resolution. The domains in the spin signal, however, are changing on the time scale of hours during repeated scanning, pointing at an influence of the magnetic tip on the observed domains. This might be attributed to the magnetically soft nature of polycrystalline Ni.

To learn more about SP-STM, its capabilities and limitations, a better defined surface than polycrystalline Ni was chosen for further studies. The (0001) surface of

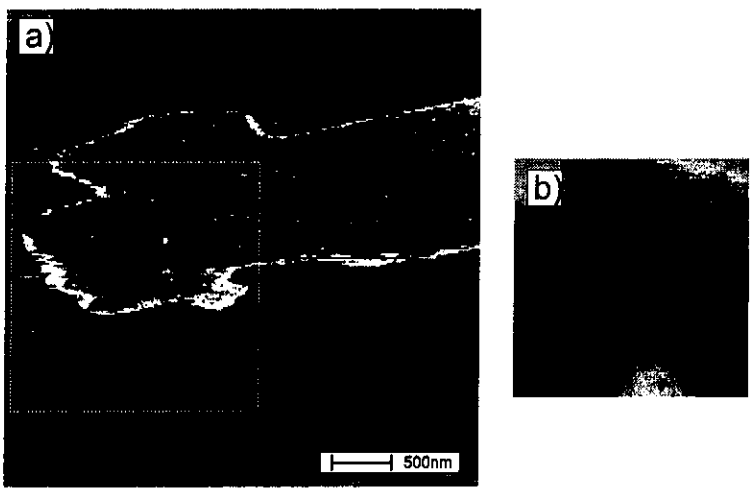

Fig. 9.6. (**a**) SP-STM scans of the spin structure of a polished polycrystalline Ni surface. To show that the observed spin contrast is not related to the morphology, the topography (**b**) and the spin signal (white box in (**a**)) of the very same area were recorded. The black-white contrast in the spin signal is 0.5% of the tunneling current. The peak-to-peak roughness of the topography corresponding to full black-white contrast is 3 nm

hcp Cobalt was investigated. Co is magnetically much harder than Ni and displays a strong uniaxial magetocrystalline anisotropy with an easy direction along the c-axis, i.e., perpendicular to the selected (0001) surface. Due to the minimization of the stray field energy, the single-domain state, however, is unstable and splits up into a Lifshitz closure domain pattern. Since for Co the magnetic anisotropy and the dipolar energy are of the same order of magnitude [22], no simple closure domain structure occurs but a complex, dendritic structure is observed [23], where the magnetization of most areas on the surface is strongly rotated away from the surface normal. Figure 9.7a shows an MFM image of the dendritic closure domain structure at the surface of Co(0001) taken in air with a tip magnetized perpendicular to the sample plane, i.e., the perpendicular magnetization component of the sample is imaged. Typical for this surface is the ramified pattern with domains that successively branch into finer structures. The magnetization flows out of and into the branches and lies almost in the surface plane between the branches. The magnetization does not have a fixed out-of-plane component, but varies continuously. As scanning electron microscopy with polarization analysis (SEMPA, see Chap. 7) measurements have shown, the perpendicular component varies between almost fully perpendicular orientation in the center of the branches to an in-plane orientation in the gray regions between the branches [23]. The refining branches of the domain pattern are an excellent object to test the experimental resolution of SP-STM. Figure 9.7b shows an SP-STM image of the typical branching structure at the same scale taken in ultrahigh vacuum from the same crystal as the MFM measurements. The domain structures observed with MFM and SP-STM are similar, although the images were not recorded on the same spot of the surface. At this magnification, the resolution limit of MFM on the order of several 10 nm to 100 nm (see Chaps. 11,12) becomes obvious. The branch structure seems to be blurred in comparison with the images taken with SP-STM at the same magnification, and the ends of the branches seem rounded, while STM shows pointed ends of the branches.

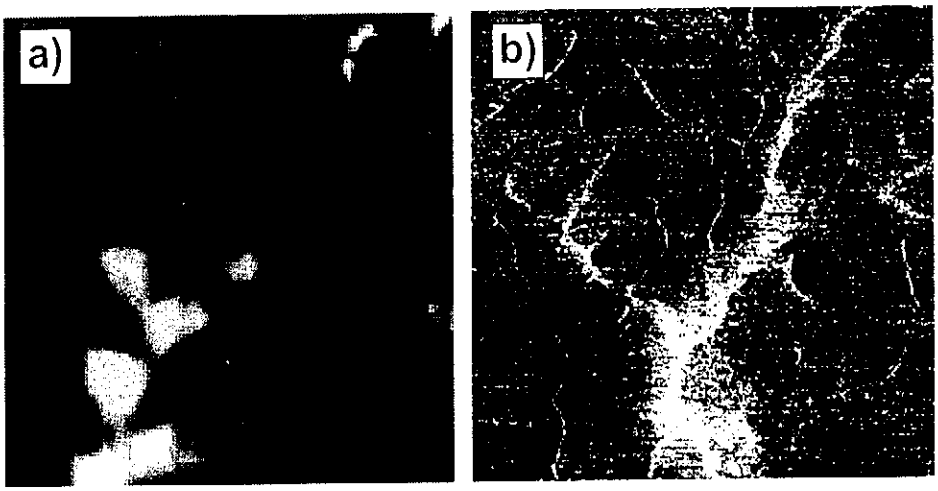

Fig. 9.7. (**a**) MFM and (**b**) SP-STM image of the closure domain pattern of Co. Both images are on the same scale of $4 \times 4\ \mu m^2$ [29]

SP-STM offers the possibility of further zooming into the closure domain structure of Co(0001) up to much higher magnifications than MFM. When focusing on the ends of the fractal branches, sharp features in the otherwise smooth contrast can be observed. The contrast across these sharp features resembles domain walls (see Fig. 9.8a). By applying a magnetic field and observing the movement of the magnetic domain wall with respect to the sample topography, it was confirmed that the contrast is indeed of magnetic origin. The contrast across the domain walls is much smaller than the full contrast observed on larger scales in the closure pattern. This can be realized when looking at the measured perpendicular magnetization component across the wall in comparison with that of the large-scale domain pattern. Figure 9.8b displays a line scan between two points of maximal contrast, i.e., between two points that are located in the center of the branches. As can be seen, the perpendicular component varies continuously along several micrometers between the two extrema. Across the domain wall at the end of a dendritic branch, the contrast changes abruptly on a length scale of about 2 nm, while the value of the change is only 20% of the maximal contrast centered just in the middle between the extrema (see Fig. 9.8c). Taking the maximal observed contrasts as perpendicular up and down magnetization, one can estimate a maximum angle of rotation across the wall of only 20° centered around the in-plane direction. To estimate the wall width w, we fit the line profile $m_z(x)$ with the standard wall profile for uniaxial systems [22]

$$m_z = \tanh(2x/w) \ , \tag{9.5}$$

resulting in the width of 1.1 ± 0.3 nm. At first sight, this ultra-narrow width seems to be unphysical and to contradict common knowledge about domain walls. The wall shown in Fig. 9.8c is one order of magnitude narrower than the Bloch wall in bulk Co of about 11 nm [22] and a factor of five narrower than the magnetic exchange length of Co. This is surprising, since the walls observed on the surface originate from bulk domains of the crystal. To exclude instrumental reasons for the

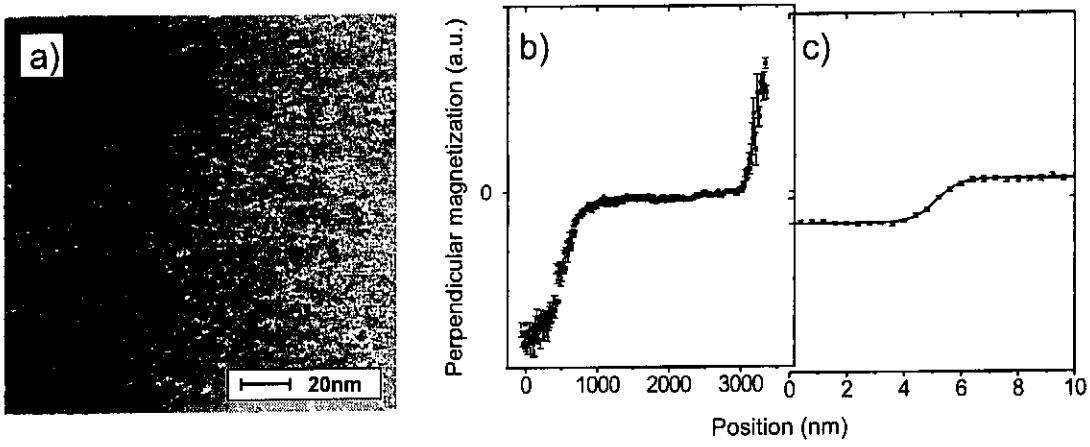

Fig. 9.8. (**a**) Detail of a sharp domain wall at an end of a branch in high magnification, (**b**) line scan through points of maximal perpendicular magnetization component, and (**c**) line scan across the ultrasharp domain wall at an end of a dendritic branch, including the fitted wall profile of 1.1 nm width

observation of such sharp walls, we take the following consideration. One mechanism that could cause sharper walls would be a nonlinear response of the instrument to the perpendicular component of the magnetization, e.g., a response like a step function. Theoretically, we can exclude such a nonlinear response, since the magneto-tunnel effect is a linear effect with the magnetization projection along the tip axis (see Eq. 9.4). Experimentally, we can exclude a step-like response function since we observe sharp and smooth contrasts in the same image, while a step-shaped response function would result in entirely sharp contrasts for all structures, including even the line scan of Fig. 9.8b. An alternative scenario could be to pick up the domain wall with the magnetic tip and drag it along during scanning until it snaps back due to the tension of the wall. In that case, a sharp transition would be observed at the point of snapping back. This is a common artifact in scanning probe techniques. To test for this mechanism, the wall was recorded while scanning from the right to the left and from the left to the right (see Fig. 9.9). If the wall was dragged along and snapped back, an opposite displacement of the wall for scanning in the two directions should have been seen. However, the domain wall appeared at exactly the same position for both directions, ruling out any significant dragging. Hence, the observed ultrasharp domain walls are real and need a physical explanation.

To understand the origin of the specific type of 20° wall and to calculate its expected width, we again focus on the closure domain pattern of Co(0001). In Co(0001) the magnetocrystalline anisotropy favors a magnetization along the surface normal. To reduce the stray field energy, domains of opposite magnetization along the normal separated by 180° domain walls are formed in the bulk of the crystal (see Fig. 9.10). This magnetization configuration reduces the overall stray field, but still produces a large number of surface charges, since the flux is not kept inside the crystal. As Hubert et al. [24] suggested, the system can reduce the amount of surface charges by a partial flux closure with tilted surface domains. In these surface domains, the magnetization rotates away from the magnetocrystalline easy direction, which cost anisotropy energy. However, the system saves dipolar energy due to the partial flux closure. For Co, the ratio between magnetocrystalline and dipolar energy is 0.4.

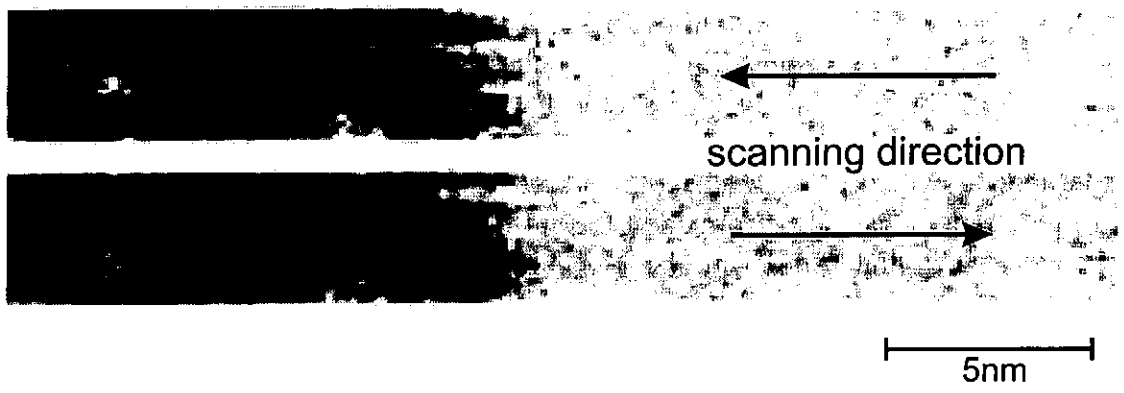

Fig. 9.9. Detailed SP-STM images of an ultra sharp domain wall scanning from the right to the left (*top*) and from the left to the right (*bottom*) excluding dragging of the domain wall during the scanning process

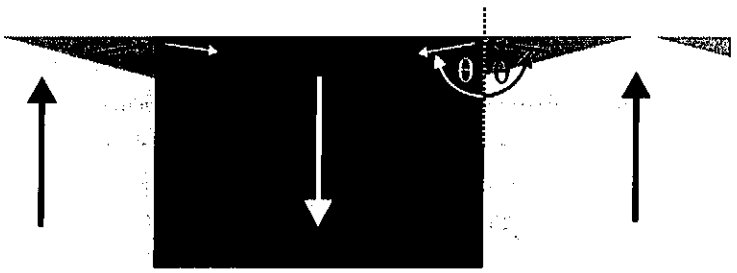

Fig. 9.10. Schematic cross section of the closure domain pattern of Co with tilted surface domains. Due to the competition of magnetocrystalline and shape anisotropy, the flux closure is incomplete at the surface and closure domains with tilted magnetization are present

From this value, one can easily calculate the angle θ, by which the magnetization is tilted from the surface normal by minimizing the free energy of the surface closure domain configuration. As depicted in Fig. 9.11a, a clear minimum of the energy at a large angle of $\theta = 80°$ is found, i.e., the flux closure is obtained by almost in-plane magnetized surface domains. Hence, under the condition that there are well-defined domains, one expects to find 20° domain walls on the surface in agreement with our SP-STM observations. Next, the expected domain wall width of such a 20° domain wall is calculated in a one-dimensional model by minimizing the sum of the magnetic exchange energy and anisotropy energy in the wall [25]. Energetic contributions of the dipolar energy are neglected in our calculation, since they only give a small correction to the wall energy. Figure 9.11b shows the wall energy as a function of the wall width w. As parameters for the calculations, the exchange constant of Co $A = 1.5 \times 10^{-11}$ J/m and the first order magnetic anisotropy of Co $K_u = 5 \times 10^5$ J/m^3 [22] were taken. The minimum of the energy is found at a wall width of only 1.5 nm. This is in good agreement with the experimentally observed wall width of 1.1 ± 0.3 nm. The small deviation of the theoretical wall widths might be due to neglecting dipolar fields or higher order anisotropies and surface anisotropies of Co(0001). This explains the occurrence and nature of the ultrasharp domain walls. There is the possibility, that a domain wall is much narrower than the magnetic exchange length $\sqrt{A/K_u}$ without violation of micromagnetic rules, but only if the angle of rotation across the wall is small. A similar wall width can be estimated by a rule of thumb argument. A 180° domain wall has a width of about 11 nm in bulk Co [22]. A 20° domain wall should have a width of a fraction of 20/180 of this. The finding of sharp domain walls on the surface of Co(0001) also gives some experimental evidence for the theoretical predictions of Hubert and Rave that sharp wall-like transitions can be formed at the surface of a closure domain pattern [26], especially when higher order in-plane or out-of-plane anisotropy terms are present, as is the case for Co(0001). Why the sharp walls are only observed close to the ends of the dendritic branches of the closure domain pattern remains an open question. Possibly only at these special points is the magnetic flux compensated in such a way that the total anisotropy term becomes stationary [26] and well-defined domains may form. For a more detailed discussion of the domain walls observed on Co(0001), see [27].

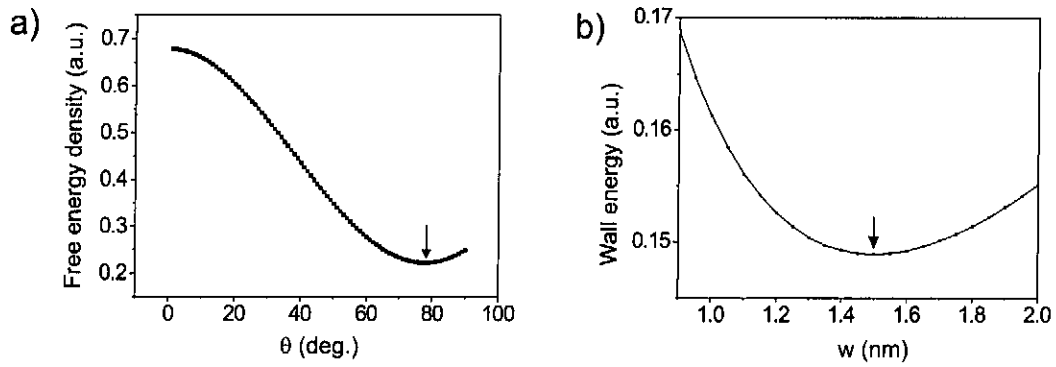

Fig. 9.11. (**a**) Free energy density of the tilted closure domain configuration as a function of the tilting angle θ [24] and (**b**) energy density as a function of width w of a 20° domain wall

9.5 Magnetic Susceptibility

With tips etched to a sharp and pointed shape, high lateral magnetic resolution of 1 nm or better can be achieved as demonstrated above with the example of a 1-nm-wide magnetic domain wall. These sharp tips are the limiting case only. In some cases, etching does not result in perfectly sharp tips as deduced from optical inspection under a microscope, or a sharp end of a tip is destroyed by a tip crash during scanning or tip approach. In these cases, the lateral resolution is worse. Besides this, there are two additional effects. After a crash, the microscopic shape of the tip is changed and by this its micromagnetic shape factor. This can result in a magnetization direction that does not lie along the tip axis anymore, and an unspecified direction of sensitivity is obtained in the magnetic contrast. The changed direction of sensitivity shows up in SP-STM images on Co as a change of the observed domain pattern from the dendritic pattern of the perpendicular magnetization to a pattern of well-defined in-plane domains similar to those in-plane domains observed on Co(0001) with SEMPA [23]. The second effect is that a dull tip produces a higher and extended magnetic stray field. In contrast to sharp tips, which produce a rather localized and limited stray field such that the domain walls of hard magnetic materials are not affected and are resolved with high resolution, the magnetic stray field of dull tips may influence the magnetic objects under investigation. The domain walls can be moved by the magnetic tips and are smeared out during imaging, or even small domains can be destroyed. In the previous section, we explained how to avoid this magnetostatic influence of the tip on the sample by using pointed tips. For dull tips, this influence is strong and magnetic imaging of undisturbed structures becomes practically impossible. The primary unwanted influence can, however, be used to measure an additional property of a magnetic sample, the local magnetic susceptibility, with high lateral resolution. As an example for a relatively dull tip, a tip cut from a piece of CoFeSiB was used. The tip was dull from optical inspection and not pointed. Nevertheless, the topographic resolution obtained with cut tips is still reasonable, as can be seen in Fig. 9.12a. Magnetic images obtained with this kind of tip often show domain walls which are smeared out over a range of up to 1 μm, as depicted in Fig. 9.12b. Note that there is a slight cross talk from the topography in the magnetic image due to

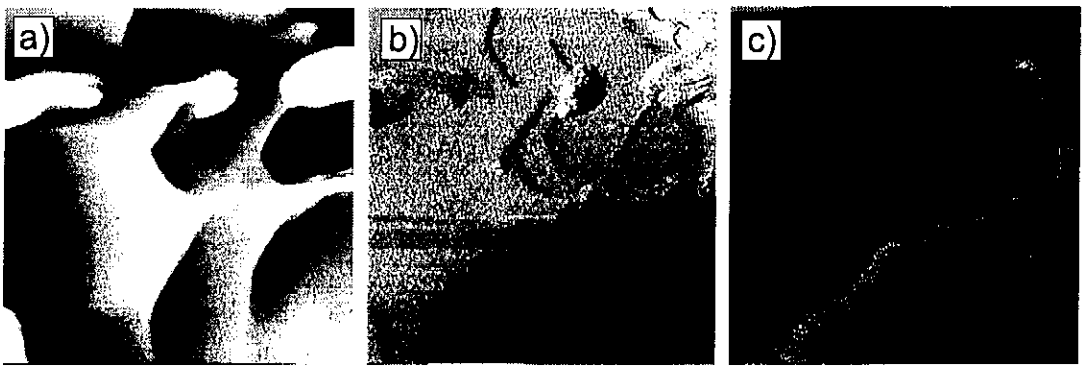

Fig. 9.12. (**a**) Topographic STM image, (**b**) magnetic image ($1f$-component) and (**c**) image of the local magnetic susceptibility ($2f$-component) of the same area on Co(0001). The switching frequency f was 41 kHz. The magnetic tip in this experiment was cut and not etched and was rather dull. All images are 8×8 μm

a somewhat higher roughness of the sample. The smearing out of the walls is due to a periodic domain wall movement induced by the alternating field of the tip. The walls rapidly oscillate with the switching frequency f such that the resolution is limited to about 1000 nm, while the topographic resolution is still good. The sample magnetization, however, cannot instantaneously follow the stray field of the tip, and a phase difference between the magnetization of the tip and the sample exists. This phase-shifted variation of the sample magnetization with frequency f induces a double frequency modulation of the tunneling current, as it is the product of the sample and tip magnetization. The higher harmonic in the tunneling current is related to the local magnetic susceptibility of the sample and can be detected simultaneously with a second lock-in amplifier with the spin signal [28]. This mechanism may be used to obtain domain wall contrast, as shown in Fig. 9.12c. From the observed width of the susceptibility signal around the wall and the switching frequency f, a local domain wall speed of around 10 cm/sec can be estimated. Hence, not only can static measurements of the sample magnetization be carried out with SP-STM, but also dynamic studies while, at the same time, recording magnetization and topography. This technique, in combination with higher switching frequencies, might even allow local studies of the switching behavior of individual magnetic nanostructures. Note that for the sharp tips described in the previous section, no measurable susceptibility signal was detected in the domain walls, showing that the magnetostatic interaction in that case can be suppressed efficiently.

9.6 The Contrast Mechanism

The difference in the lateral resolution of the two scanning probe techniques, MFM and SP-STM, is based on the physical phenomena underlying their contrast mechanisms. In MFM, the force between the magnetic volume of the end of the tip and the sample is used. In order to minimize the cross talk from the topography in the magnetic image, the tip is positioned several tens of nanometers above the sample

during magnetic imaging. Due to the size of the effective magnetic volume of the tip, as well as the distance between the magnetic center of that volume and the sample surface, magnetic forces are averaged over a large region, which limits the lateral resolution. As discussed in Chaps. 11 and 12, the upper resolution limit is on the same order as the distance between the magnetic center of the tip and the sample surface, i.e., it is typically several tens of nanometers. In SP-STM, the spin-polarized tunneling current between the surface of the sample and the apex of the tip is used to obtain magnetic information. Here, the resolution is only limited by the sharpness of the tip, which can be atomic under favorable circumstances. Above, we demonstrated a resolution of at least 1 nm, which is impossible to obtain with an MFM using bulk magnetic CoFeSiB tips, since the magnetic volume of the tip is extremely large. As a price for the better resolution of SP-STM, however, the contrast mechanism requires clean samples and tips and imaging has to be carried out under ultrahigh vacuum conditions. The exposure of the clean sample surface and tip to just 10 Langmuir of molecular oxygen leads to a practically complete vanishing of magnetic contrast showing the high surface sensitivity of the contrast mechanism. For a more detailed comparison of the contrast mechanisms of SP-STM and MFM, see [29].

Besides high resolution magnetic imaging, SP-STM can also be used to learn more about the fundamental physics of its contrast mechanism, i.e., the tunneling magnetoresistance effect across a vacuum barrier. The technique allows continuous variations of parameters that are inaccessible in planar junctions with oxide barriers. Here, we focus on the dependence of the TMR on the barrier resistance. In SP-STM, the resistance can be continuously varied by choosing the feedback parameters, i.e., the tunneling voltage and the current, for the topographic stabilization of the tip. Recording the observed magnetic contrast across a domain wall of Co(0001) as a function of feedback current and fixed voltage, the TMR as a function of resistance is measured. As depicted in Fig. 9.13, one notices a more or less constant TMR above resistances of $10^7\ \Omega$ and a continuous drop below $10^7\ \Omega$. First of all, this

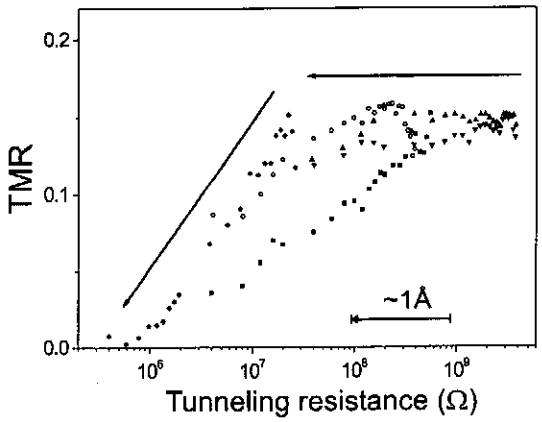

Fig. 9.13. Size of tunneling magnetoresistance (TMR) as a function of resistance of the tunneling gap. The arrows are guides to the eye only. Different symbols represent measurements with different tips and different bias voltages between 20 and 1000 mV. The strongest drop is observed for bias voltages around 200 mV

dependence gives a guideline – what feedback parameters to use in SP-STM to get an optimal magnetic contrast. One should avoid resistances below $10^7\ \Omega$. Secondly, one may learn more about the TMR effect itself. When increasing the tunneling current and, by this, approaching the tip toward the surface (one order of magnitude in the tunneling resistance corresponds roughly to an approach of 1 Å), the TMR effect starts to decrease below a critical gap width. This is in contrast to Jullière's model, which predicts that the TMR effect is only a function of the spin polarization of the two ferromagnets and not a function of the gap width. The same holds for the more elaborate model of Slonczewski (see Eq. 9.4), where only the average conductance G_0 depends on the gap width. However, Slonczewski predicted that the TMR in the free electron approximation depends on the barrier height [4], as the effective polarization of the electrodes P_i' not only contains information of the ferromagnet, but also information of the barrier. P_i' is given by

$$P_i' = (k_\uparrow - k_\downarrow)/(k_\uparrow + k_\downarrow) * (\kappa^2 - k_\uparrow k_\downarrow)/(\kappa^2 + k_\uparrow k_\downarrow) \tag{9.6}$$

where $k_\uparrow$ and $k_\downarrow$ are the momenta of the majority/minority electrons at the Fermi energy and κ the imaginary momentum of the electrons in the barrier, which is directly related to the barrier height Φ. The first factor of equation 9.6 reflects the

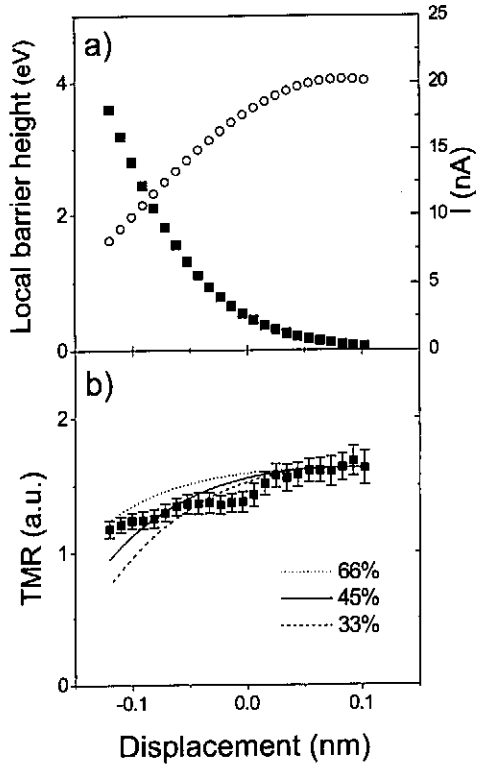

Fig. 9.14. (**a**) Filled squares show the tunneling current as a function of displacement, where negative displacements correspond to an approach of the tip. The open circles are the barrier height of the gap calculated from the tunneling current. (**b**) Filled squares represent the measured TMR as a function of displacement, while the lines are the TMRs calculated with the measured barrier heights and the spin polarizations as indicated. All TMR values have been normalized to the TMR at large distance (0.1 nm displacement)

spin polarization of the free electron gas at the Fermi energy, while the second factor is a correction factor that is related to the ferromagnet/insulator matching. Hence, one can expect that experimentally the TMR effect depends on the barrier height. To measure the barrier height of the vacuum barrier between tip and sample as a function of the gap width S, the tunneling current I as a function of the displacement was recorded, as depicted in Fig. 9.14a. The barrier height Φ can be determined from

$$\Phi(\mathrm{eV}) = 0.952(\mathrm{d}\ln(I)/\mathrm{d}S)^2 \tag{9.7}$$

for small bias voltages [30]. Indeed one observes a drop of Φ when coming closer than the corresponding gap resistance of $\sim 5 \times 10^7\ \Omega$ (see Fig. 9.14a). Simultaneous to the tunneling current, the TMR effect was recorded as shown in Fig. 9.14b. It displays the characteristic decrease below $10^7\ \Omega$. Using Slonczewski's model with a spin splitting of 1 eV for Co [31] and a spin polarization of 45% [17], the distance dependence of the effective polarization P_i' and the TMR can be calculated from the experimentally observed barrier height. The result for the TMR is plotted as a solid line in Fig. 9.14b, showing good agreement with the measured TMR as a function of the gap width. Therefore, the drop of the TMR at small gap width can be attributed to the reduction of the barrier height. For comparison, we also calculated the expected drop of the TMR for 33% and 65% spin polarization. Qualitatively, the same drop is observed. The reduction of the barrier height at resistances below $10^7\ \Omega$ has been observed also for other surfaces [21,30] and can be attributed to the overlap of electron densities of tip and sample at short distances [30]. Due to the overlap, electrons do not have to overcome the whole work function to go from one electrode to the other, but feel only a fraction of it. Since this effect is rather fundamental, one should expect that the TMR decreases for other materials, as well when the tip is approached, giving a general rule for optimal magnetic imaging conditions. For a more detailed discussion of this effect, see [32].

Finally, we discuss the possibility of observing magnetic domains through a thin overlayer of a nonmagnetic material, e.g., Au(111). For the case of planar tunneling junctions, the use of a nonmagnetic layer inserted between the insulator barrier and one of the ferromagnetic electrodes has been studied intensively [33–36]. Conflicting results for the dependence of the TMR on the thickness of the nonmagnetic spacer layer have been reported. The TMR was found to decay very rapidly with the overlayer thickness [34, 35] such that only a couple of atomic layers led to the complete vanishing of spin polarization, while others find a much slower decay [33]. It has been shown that the decay is different when the layer is inserted between the bottom electrode and the insulator or above the insulator, hinting at an influence of different growth morphologies of the spacer layer [36]. Several groups have also addressed this problem from the theoretical side [37–40], showing a rather slow decay of the spin polarization of the tunneling current with overlayer thickness. For magnetic imaging with SP-STM, nonmagnetic overlayers of noble metals may be used to protect the ferromagnetic sample from oxidation in air. If imaging is possible through the overlayer, operation under ambient conditions could be possible with an inert tip. To test the theoretical predictions for the idealized structures and achieve magnetic imaging through a protective layer, we deposited a thin Au film on top of the Co(0001)

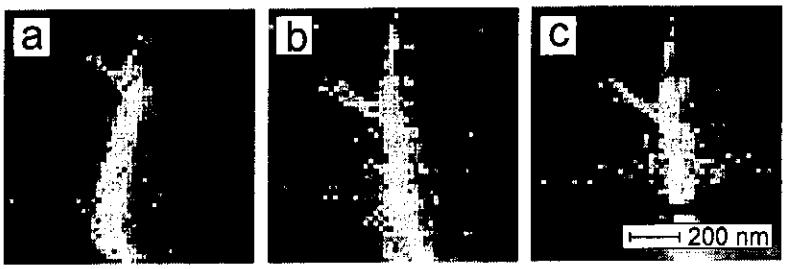

Fig. 9.15. SP-STM images of nearly the same area of a Co(0001) crystal at different Au overlayer thicknesses. (**a**) clean Co(0001), (**b**) 1.3 ML Au, (**c**) 2.6 ML Au. The contrast only weakly decreases with Au coverage

single crystal. As LEED images show, the Au film is single crystalline and grows in the (111) orientation on Co. STM images at different coverages revealed an almost perfect layer-by-layer growth. Since the domain structure of Co is rather complex and different domains of different contrast can be observed, we carried out the measurements of the contrast as a function of Au overlayer thickness on the same magnetic domain. For this, an Au evaporator was installed such that deposition is possible under glancing incidence underneath the tip while the tip is retracted by a couple of micrometers. After deposition, the tip is approached again and the very same area can be imaged. Figure 9.15 shows the magnetic images after a series of depositions. Interestingly, the contrast is found to decay only weakly with Au thickness. Hence, imaging through a protective layer is possible, and the theoretical predictions are confirmed by our experiment. The slow decay of the spin polarization of the tunneling electrons can be explained by a spin-scattering length that usually even exceeds the mean free path of the electrons in Au on the order of several tens of nanometers [41].

9.7 Conclusions and Outlook

Magnetic imaging utilizing scanning tunneling microscopy with ferromagnetic tips has been presented. It is a technique with high lateral resolution of at least 1 nm for both topographic and magnetic information, which can be separated sufficiently well regardless of the crystallographic or electronic structure of the sample due to a modulation of the magnetization of the tip. In contrast to magnetic force microscopy, it directly measures one of the magnetization components of the sample surface, usually the perpendicular component. The technique, however, requires relatively high experimental efforts, i.e., special tips and atomically clean sample surfaces, to achieve magnetic contrast. The possibility of imaging the magnetization of a sample through a thin Au film might lead to less stringent requirements for magnetic imaging in the future. Similar to magnetic force microscopy, the use of a magnetic tip causes stray fields that can influence the sample magnetization under unfavorable conditions. However, the modulation technique allows one to check for an influence during imaging and to use this influence to locally measure the magnetic susceptibility. In

the future, the development of tips of other shapes, e.g., ring-shaped tips, might allow one to purely measure in-plane magnetic components of a well-defined direction. In that case, the influence of the stray field of the tip might also be reduced.

Acknowledgement. I would like to thank Mrs. Chen Chen and especially Haifeng Ding for their patience in carrying out many of the experiments presented here, Riccardo Hertel for the micromagnetic modeling of the tip, Gerold Steierl for SEM images, Manuel Vazquez for providing the amorphous wires, and Jürgen Kirschner for his support and many hints and discussions. Furthermore, I would like to thank Olivier Fruchard, Jian Shen, Hans Peter Oepen, and Patric Bruno for helpful suggestions, and Wolfgang Kuch for his critical reading of the manuscript. Finally, I wish to thank Yoshishige Suzuki for the kind permission to show his material.

References

1. G. Binning, H. Rohrer, Ch. Gerber, and E. Weibel, Appl. Phys. Lett. **40**, 178 (1982).
2. G. Binning, H. Rohrer, Ch. Gerber, and E. Weibel, Phys. Rev. Lett. **49**, 57 (1982).
3. M. Jullière, Phys. Lett. **54A**, 225 (1975).
4. J.C. Slonczewski, Phys. Rev. B **39**, 6995 (1989).
5. T. Miyazaki and N. Tezuka, J. Magn. Magn. Mater. **139**, L231 (1995).
6. D.T. Pierce and F. Meier, Phys. Rev. B **13**, 5484 (1976).
7. M. Johnson and J. Clarke, J. Appl. Phys. **67**, 6141 (1990).
8. R. Wiesendanger, H.J. Güntherodt, G. Güntherodt, R.J. Gambino, and R. Ruf, Phys. Rev. Lett. **65**, 247 (1990).
9. S. Blügel, D. Pescia, and P.H. Dederichs, Phys. Rev. B **39**, 1392 (1989).
10. M.W.J. Prins, R. Jansen, and H. van Kempen, Phys. Rev. B **53**, 8105 (1996).
11. Y. Suzuki, W. Nabhan, and K. Tanaka, Appl. Phys. Lett. **71**, 3153 (1997).
12. H. Kodama, T. Uzumaki, M. Oshiki, K. Sueoka, and K. Mukasa, J. Appl. Phys. **83**, 6831 (1998).
13. M.W.J. Prins, R.H.M. Groeneveld, D.L. Abraham, H. van Kempen, and H.W. van Kersteren, Appl. Phys. Lett. **66**, 1141 (1995).
14. Y. Suzuki, W. Nabhan, R. Shinohara, K. Yamaguchi, and T. Katayama, J. Magn. Magn. Mater. **198–199**, 540 (1999).
15. M. Bode, M. Getzlaff, and R. Wiesendanger, Phys. Rev. Lett. **81**, 4256 (1998).
16. W. Wulfhekel and J. Kirschner, Appl. Phys. Lett. **75**, 1944 (1999).
17. J.S. Moodera, and G. Mathon, J. Magn. Magn. Mater. **200**, 248 (1999).
18. Magnetic wires were kindly provided by M.Vazquez.
19. J. Velazquez, M. Vazquez, D.-X. Chen, and A. Hernando, Phys. Rev. B **50**, 16737 (1994).
20. H. Theuss, B. Hofmann, C. Gómez-Polo, M. Vázquez, and H. Kronmüller, J. Magn. Magn. Mater. **145**, 165 (1994).
21. Y. Kuk and P.J. Silverman, J. Vac. Sci. Technol. A **8**, 289 (1990).
22. E. Kneller, *Ferromagnetismus*, Springer-Verlag, Berlin (1962).
23. J. Unguris, M.R. Scheinfein, R.C. Celotta, and D.T. Pierce, Appl. Phys. Lett. **55**, 2553 (1989).
24. A. Hubert and R. Schäfer, *Magnetic Domains*, Springer-Verlag, Berlin, p. 315 (1998).
25. A. Aharoni, *Introduction to the Theory of Ferromagnetism*, Oxford University Press, New York (1996).

26. A. Hubert and W. Rave, J. Magn. Magn. Mater. **196–197**, 325 (1999).
27. H.F. Ding, W. Wufhekel, and J. Kirschner, Europhys. Lett. **57**, 100 (2002).
28. W. Wulfhekel, H.F. Ding, and J. Kirschner, J. Appl. Phys. **87**, 6475 (2000).
29. H.F. Ding, W. Wulfhekel, C. Chen, and J. Kirschner, Material Science & Engeneering B **84**, 96 (2001).
30. A. Sakai In: T. Sakurai, Y. Watanabe (eds) *Advances in Scanning Probe Microscopy*, Springer, pp. 143 (1999).
31. M.B. Stearns, J. Magn. Magn. Mater. **5**, 167 (1977).
32. H.F. Ding, W. Wulfhekel, and J. Kirschner, J. Magn. Magn. Mater. **242–245**, 47 (2002).
33. J.S. Moodera, M.E. Taylor, and R. Meservey, Phys. Rev. B **40**, 11980 (1989).
34. J.S. Moodera, J. Nowak, L.R. Kinder, P.M. Tedrow, R.J.M. van de Veerdonk, B.A. Smits, M. van Kampen, H.J.M. Swagten, and W.J.M. de Jonge, Phys. Rev. Lett. **83**, 3029 (1999).
35. J.J. Sun and P.P. Freitas, J. Appl. Phys. **85**, 5264 (1999).
36. P. LeClair, H.J.M. Swagten, J.T. Kohlhepp, R.J.M. van de Veerdonk, W.J.M. de Jonge, Phys. Rev. Lett. **84**, 2933 (2000).
37. A. Vedyayev, N. Ryzhanova, C. Lacroix, L. Giacomoni, and B. Dieny, Europhys. Lett. **39**, 219 (1997).
38. W.S. Zhang, B.Z. Li, and Y. Li, Phys. Rev. B **58**, 14959 (1998).
39. S. Zhang, P.M. Levy, Phys. Rev. Lett. **81**, 5660 (1998).
40. J. Mathon and A. Umerski, Phys. Rev. B **60**, 1117 (1999).
41. M.K. Weilmeier, W.H. Rippard, and R.A. Buhrman, Phys. Rev. B **59**, R2521 (1999).